

# Revealing Activity Trends of Metal Diborides Toward pH-Universal Hydrogen Evolution Electrocatalysts with Pt-Like Activity

Qiuju Li, Xu Zou, Xuan Ai, Hui Chen, Lei Sun, and Xiaoxin Zou\*

Understanding of catalytic trends is an important prerequisite for providing rational guidance toward the prediction of advanced catalysts as well as the development of original materials design principles. A combined theoretical and experimental study that reveals the periodic trends in electrocatalytic activity for the hydrogen evolution reaction (HER) from Group IV B to Group VIII metal diborides is reported here. Theoretical results demonstrate a general linear relationship between the catalytic activity and *d*-band center of metal diboride, meaning that the latter can serve as a descriptor of activity. And theoretical results also predict ruthenium diboride as the most competitive, nonplatinum candidate among metal diborides for HER because this material has a suitable *d*-band center and a high density of efficient active sites. Furthermore, the experimental results validate the theoretical activity trends and identify ruthenium diboride as an efficient, pH-universal electrocatalyst with Pt-like activity for HER under both acidic and alkaline media.

benchmark HER catalyst—is such a material possessing an appropriate hydrogen adsorption free energy. Over the past several years, many efforts have been devoted to: i) improve platinum's catalytic activity by subjecting it to some chemical treatments,<sup>[2]</sup> such as surface modification, alloying, and heteroatom doping, and ii) completely replace it with alternative nonplatinum catalysts, such as transition metal alloys, sulfides, carbides, nitrides, and borides.<sup>[1,3–7]</sup> Despite some progresses in HER catalysts, most of these catalysts were developed by a cost-intensive, time-consuming trial-and-error approach. Hence, it is important to better understand the activity trends for a given class of materials that can ultimately providing clear guide to more accurately and rapidly discover new advanced catalysts for HER.

## 1. Introduction

The hydrogen evolution reaction (HER) is of technological importance, as often stressed in many fields such as water electrolysis, chlor-alkali electrolysis, etc.<sup>[1]</sup> This reaction is also of fundamental significance because it is often considered as a model reaction for the investigation of electrochemical mechanism and kinetics.<sup>[1]</sup> The HER is a classic two-electron reduction process with  $H^*$  as the only reaction intermediate ( $2H^+ + 2e^- \rightarrow H_2$  in acidic solution or  $2H_2O + 2e^- \rightarrow H_2 + 2OH^-$  in alkaline solution). According to Sabatier principle, an active HER catalyst generally binds  $H^*$  neither too weakly nor too strongly, regardless of the pH value of reaction solution. Platinum—the

Compared with the prominent transition metal disulfide catalysts (e.g.,  $MoS_2$ ),<sup>[3a,8]</sup> transition metal diborides (i.e.,  $MoB_2$ ) with the 3D metallic framework and 2D boron layers as subunits (also known as borophene subunits) have recently emerged as a potential new frontier for searching better HER catalysts.<sup>[9]</sup>  $MoB_2$ , a representative example, has been reported to demonstrate promising HER activity thanks to its better electronic conductivity and more abundant catalytic sites relative to  $MoS_2$ .<sup>[9a]</sup> While a family of metal diborides with well-defined crystal structures are available, the catalytic activities for HER of most of them are unknown. Additionally, despite their potential advantages, transition metal diboride catalysts progress significantly more slowly than other types of HER catalysts (e.g., metal disulfides). The slow development of metal diboride catalysts is mainly because of their inherent synthesis difficulties and current poor knowledge on design principles for this new kind of materials.

Herein, we present an investigation of the electrocatalytic activities for HER on a family of 12 transition metal diborides both theoretically and experimentally. The electrocatalytic activity is found to generally increase from Group IV B to Group VIII metal diborides, and can be described as a function of the *d*-band center of metal diboride (i.e., an activity descriptor). The coupling interactions between metal *d*-orbitals and boron *sp*-orbitals makes the *d*-orbitals center of metal diborides downshift away from Fermi level, resulting in an optimized  $H^*$  adsorption or a better catalytic activity. Finally, our

Q. Li, X. Zou, X. Ai, Dr. H. Chen, Prof. X. Zou  
State Key Laboratory of Inorganic Synthesis and Preparative Chemistry  
College of Chemistry  
Jilin University  
Changchun 130012, P. R. China  
E-mail: xzou@jlu.edu.cn

Prof. L. Sun  
State Key Laboratory of Molecular Reaction Dynamics  
Dalian Institute of Chemical Physics  
Dalian 116023, P. R. China

 The ORCID identification number(s) for the author(s) of this article can be found under <https://doi.org/10.1002/aenm.201803369>.

DOI: 10.1002/aenm.201803369

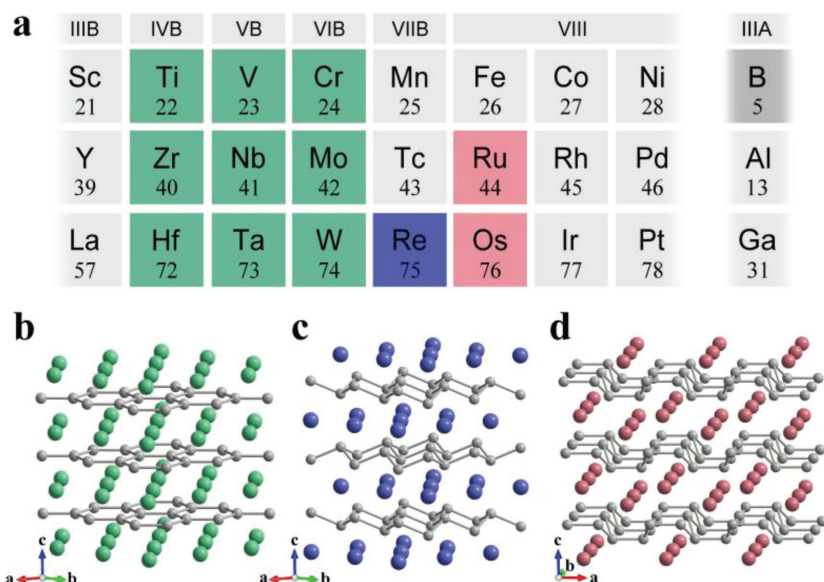


**Figure 1.** a) A schematic of the periodic table with a highlight of the 12 transition metal elements that are used for constructing transition metal diborides. Crystal structures of b)  $\text{AlB}_2$ -type diborides, c)  $\text{ReB}_2$ -type diboride, and d)  $\text{RuB}_2$ -type diborides. Color codes: grey is boron, green is the metal constructing the  $\text{AlB}_2$ -type diborides, blue is the metal constructing the  $\text{ReB}_2$ -type diboride, pink is the metal constructing the  $\text{RuB}_2$ -type diboride.

combined theoretical and experimental results identify ruthenium diboride as a novel, very competitive, nonplatinum electrocatalyst for HER in both acidic and alkaline solutions.

site on metal-terminated (001) surface of the 12  $\text{MB}_2$  (see Figure S1 and Tables S1–S5 in the Supporting Information). The calculation results (see the Y-axis of Figure 2a) reveal that the absolute value of  $\Delta G_{\text{H}^*}$  generally decreases in the order: Group VIII-diborides (i.e.,  $\text{RuB}_2$ ,  $\text{OsB}_2$ ) < Group VII B-diboride (i.e.,  $\text{ReB}_2$ ) < Group VI B-diborides (i.e.,  $\text{CrB}_2$ ,  $\text{MoB}_2$ ,  $\text{WB}_2$ ) < Group V B-diborides (i.e.,  $\text{VB}_2$ ,  $\text{NbB}_2$ ,  $\text{TaB}_2$ ) < Group IV B-diborides (i.e.,  $\text{TiB}_2$ ,  $\text{ZrB}_2$ ,  $\text{HfB}_2$ ). This trend further suggests that the HER activity of these  $\text{MB}_2$  increases monotonically from Group IV B to Group VIII metal diborides, with  $\text{RuB}_2$  as the most promising candidate for HER among  $\text{MB}_2$ .

The above periodic trends in activity inspire us to correlate the HER activity to the electronic structure of  $\text{MB}_2$ , particularly the metal  $d$ -orbital characters. We calculated the density of states (DOS) for metal  $d$ -states in the 12  $\text{MB}_2$  (Figures S2 and S3, Supporting Information), and presented their  $d$ -band centers in the X-axis of Figure 2a. As shown in Figure 2a, there is, in general, a linear correlation between  $\Delta G_{\text{H}^*}$  and  $d$ -band center. Such a linear correlation is especially clear for those  $\text{MB}_2$  based on transition metal elements from the same period (Figure S4, Supporting Information), whose  $\Delta G_{\text{H}^*}$  values decreases almost linearly as the  $d$ -band center of  $\text{MB}_2$  shifts to a more negative value for  $\text{MB}_2$ . This can be

## 2. Results and Discussion

Figure 1a presents a schematic of the periodic table with a highlight of the 12 transition metal elements that are used for constructing transition metal diborides ( $\text{MB}_2$ ) with well-defined crystal structures.<sup>[10]</sup> These  $\text{MB}_2$  can be classified into three structure types (Figure 1b–d), including nine  $\text{AlB}_2$ -type diborides ( $M = \text{Ti, Zr, Hf, V, Nb, Ta, Cr, Mo, and W}$ ), one  $\text{ReB}_2$ -type diboride ( $M = \text{Re}$ ), and two  $\text{RuB}_2$ -type diborides ( $M = \text{Ru and Os}$ ). While the boron atoms are covalently bonded into graphene-like boron layers in  $\text{AlB}_2$ -type diborides, the boron layers feature cyclohexane-like “chair” and “boat” conformations in  $\text{ReB}_2$ -type and  $\text{RuB}_2$ -type diborides, respectively.

We evaluated theoretically catalytic activity for HER of the 12  $\text{MB}_2$  based on the Gibbs free energy ( $\Delta G_{\text{H}^*}$ ) of atomic H bonding to a given catalytic site.  $\Delta G_{\text{H}^*}$  is a widely accepted indicator of HER activity for a given catalytic site, with a smaller absolute value indicating a better catalytic activity.<sup>[8]</sup> Under the optimal condition of  $\Delta G_{\text{H}^*} \approx 0$ , the best HER activity is obtained. We calculated  $\Delta G_{\text{H}^*}$  for H atom adsorbed at the most energetically favorable

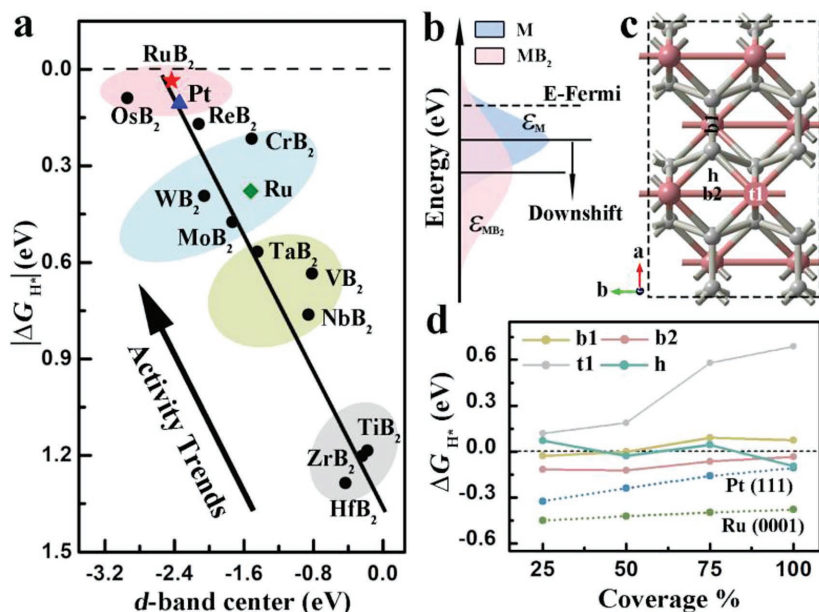


**Figure 2.** a) Fitted linear relationship between hydrogen adsorption free energy ( $\Delta G_{\text{H}^*}$ ) and  $d$ -band center of  $\text{MB}_2$ , Pt, and Ru. b) Schematic explanation of the boron effect on the  $d$ -bands of metal.  $\epsilon_M$  and  $\epsilon_{\text{MB}_2}$  represent  $d$ -band centers of metal and metal diboride, respectively. c) The stable adsorption sites for  $\text{H}^*$  on  $\text{RuB}_2(001)$  surface. d)  $\Delta G_{\text{H}^*}$  for the  $\text{RuB}_2(001)$  surface as a function of hydrogen coverage. The top, bridge, and hollow sites are denoted with “t”, “b,” and “h,” respectively. And b1 and b2 represent the different kinds of bridge sites.  $\Delta G_{\text{H}^*}$  for the Pt(111) and Ru(0001) surfaces are also included in the figure.

explained by the fact that when the  $d$ -band center becomes more negative relative to Fermi level, antibonding states will shift to lower energy and become more occupied.<sup>[11]</sup> This, thus, will benefit for the decrease in the binding energy for H atom (i.e.,  $\Delta G_{H^*}$ ).<sup>[11]</sup> The above results suggest that the  $d$ -band center can serve as a descriptor for predicting the HER catalytic activity of MB<sub>2</sub>.

The above results also make us identify RuB<sub>2</sub> as the most active material for HER among MB<sub>2</sub> we studied. For comparison, the catalytic activities of metallic Pt and Ru are investigated theoretically. Figure 2a presents the  $d$ -band centers and the  $\Delta G_{H^*}$  values for Pt(111) and Ru(0001) surfaces, which are often investigated as model surfaces of Pt and Ru for density functional theory (DFT) calculations.<sup>[12]</sup> In comparison with Pt, RuB<sub>2</sub> has a little lower  $d$ -band center and smaller absolute value of  $\Delta G_{H^*}$ , suggesting that RuB<sub>2</sub> might have a higher catalytic activity than Pt. In addition, RuB<sub>2</sub> exhibits an obviously lower  $d$ -band center and much smaller absolute value of  $\Delta G_{H^*}$  compared with Ru, demonstrating the importance of boron atoms in enhancing HER activity. As illustrated in Figure 2b, the bandwidth of metal  $d$ -band in RuB<sub>2</sub> (7.18 eV<sup>2</sup>) becomes broader relative to the corresponding metallic Ru (5.04 eV<sup>2</sup>), owing to the coupling interactions between metal  $d$ -orbitals and boron  $sp$ -orbitals. Meanwhile, the number of occupied metal  $d$ -states remains unchanged between Ru and RuB<sub>2</sub> as calculated by the number of  $d$ -electrons per surface Ru atom. The broadened  $d$ -band, coupled with the unchanged  $d$ -band filling, makes the  $d$ -band center of RuB<sub>2</sub> downshift away from Fermi level, resulting in a smaller  $\Delta G_{H^*}$  or a better catalytic activity.

We further compared the calculation results of RuB<sub>2</sub>, Pt, and Ru in a more detailed way. The stable sites for H adsorption among possible sites on the RuB<sub>2</sub> (001) surface (Figure S1c, Supporting Information) include a top site (t1) over Ru atom, two bridge sites (b1 and b2) over B–B bond and Ru–Ru bond, respectively, and a hollow site (h) over a ring on the surface (Figure 2c). The  $\Delta G_{H^*}$  values for the t1, b1, b2, and h sites in a range of H coverage ( $\theta_{H^*}$ ) from 25% to 100% ML are presented in Figure 2d. For comparative purpose, the  $\Delta G_{H^*}$  values as a function of  $\theta_{H^*}$  for the Pt(111) and Ru(0001) surfaces are also involved in the Figure 2d. The results show that the b1, b2, and h sites on the RuB<sub>2</sub>(001) surfaces exhibit near-zero  $\Delta G_{H^*}$  absolute values throughout the whole  $\theta_{H^*}$  range, which are even smaller than those for the Pt(111) and Ru(0001) surfaces. These results suggest that RuB<sub>2</sub> contains a large density of highly active catalytic sites for HER.

To validate the theoretical activity trends, careful synthesis and experimental tests of these MB<sub>2</sub> are required. Although some conventional methods have been developed for the preparation of metal borides,<sup>[9,10,13]</sup> the general and selective synthesis of metal diborides still remains a challenge. Here, we synthesized a family of MB<sub>2</sub> nanomaterials (M = Ti, Zr, Hf, V, Nb, Ta, Cr, Mo, W, Re, Ru, and Os) by employing a quasi solid-state metathesis (SSM) reaction<sup>[14]</sup> between magnesium diboride (MgB<sub>2</sub>) and anhydrous metal chloride (see experimental details in Experimental Section and Table S6 in the Supporting Information).

As shown in Figure 3, the majority of MB<sub>2</sub> we synthesized are high purity (M = Ti, Zr, Hf, V, Nb, Ta, Mo, Re, and Ru), with the exception of WB<sub>2</sub> (denoted as WB<sub>x</sub>), CrB<sub>2</sub> (denoted

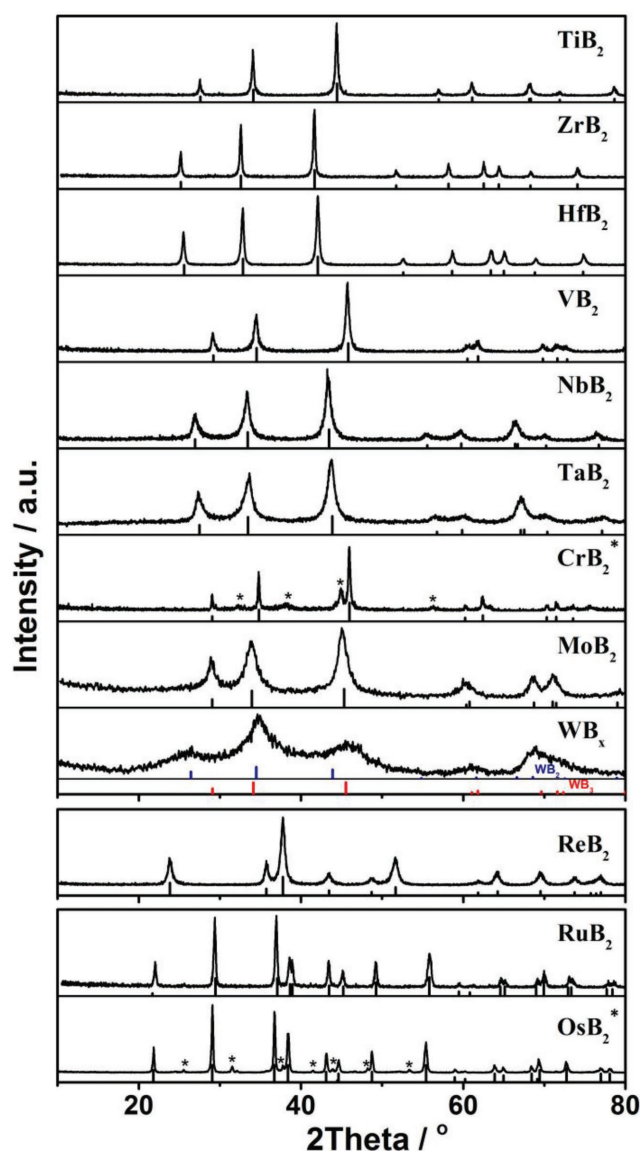


**Figure 3.** The XRD patterns of MB<sub>2</sub>. Especially, the “\*” in the XRD pattern of CrB<sub>2</sub>\* indicates the XRD peaks of the impurity phase CrB; and the “\*” in the XRD pattern of OsB<sub>2</sub>\* indicates an unknown impurity phase. Blue lines and red lines are the XRD peak positions of WB<sub>2</sub> and WB<sub>3</sub>. Data for these peak positions derived from references [15a,b].

as CrB<sub>2</sub>\*), and OsB<sub>2</sub> (denoted as OsB<sub>2</sub>\*). Powder X-ray diffraction (XRD) results reveal that OsB<sub>2</sub>\* and CrB<sub>2</sub>\* contain some impurity phases, while peak positions of WB<sub>x</sub> deviate from the standard XRD pattern of WB<sub>2</sub> or WB<sub>3</sub>.<sup>[15]</sup> Transmission electron microscopy (TEM) images (Figure S5, Supporting Information) show that most of MB<sub>2</sub> are composed of closely packed nanoparticles with average size ranging from 13.7 to 110.5 nm, with the exception of ReB<sub>2</sub> consisting of nanoparticles with irregular shape. Additionally, Brunauer–Emmett–Teller (BET) surface areas of these MB<sub>2</sub> are found to be between 6.4 and 42.3 m<sup>2</sup> g<sup>−1</sup> (see Table S7 in the Supporting Information). These results illustrate that the SSM reaction provides a general strategy to controllably obtain MB<sub>2</sub>. Moreover, this method also can be extended to synthesis some metal borides with different



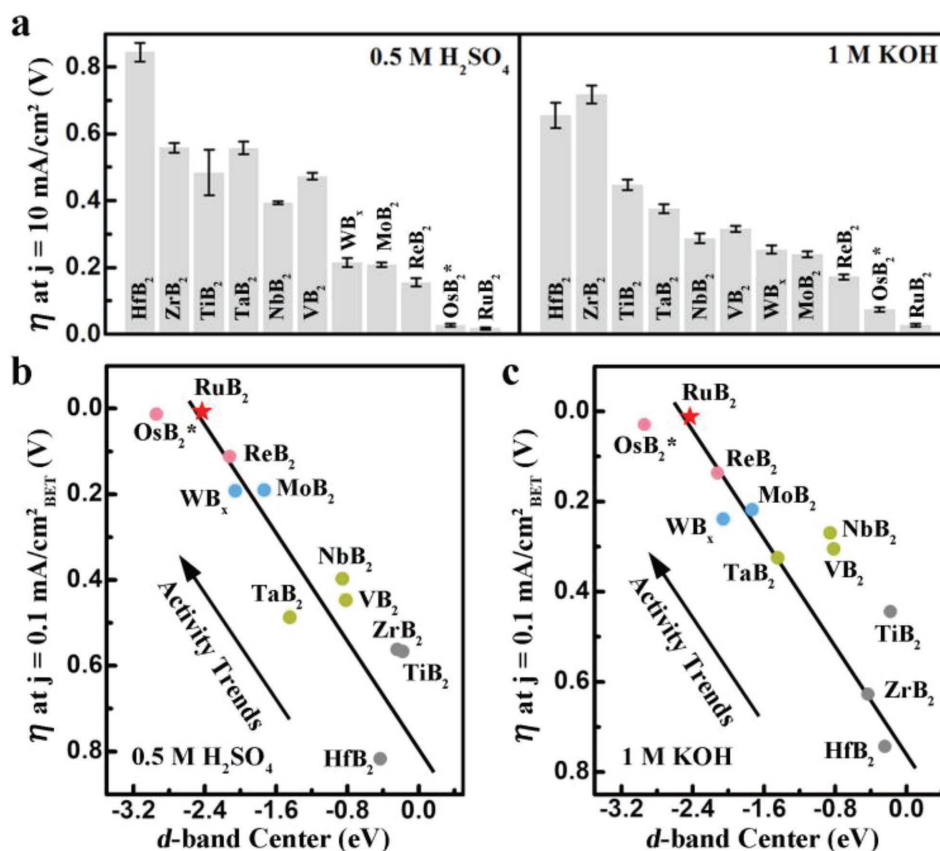


**Figure 4.** The experimental HER activity of MB<sub>2</sub> in acidic and alkaline media. a) Overpotentials required at a current density of  $10 \text{ mA cm}^{-2}$  in  $0.5 \text{ M H}_2\text{SO}_4$  solution (left) and  $1.0 \text{ M KOH}$  solution (right). The current density was normalized with the geometric surface area of the electrode. Error bars indicate standard deviation from five measurements. b,c) Fitted linear relationship between the measured overpotential and  $d$ -band center at a current density of  $0.1 \text{ mA cm}^{-2}$  (normalized by BET surface area) in  $0.5 \text{ M H}_2\text{SO}_4$  solution and  $1.0 \text{ M KOH}$  solution.

stoichiometry such as FeB, NiB, and MnB<sub>4</sub> (Figure S6, Supporting Information).

After synthesis, we measured electrocatalytic activities of MB<sub>2</sub> toward HER (see experimental details in Experimental Section). Note that CrB<sub>2</sub> is soluble in acidic solution, and thus was not investigated further. **Figure 4a** presents the overpotentials required to reach the current density of  $10 \text{ mA cm}^{-2}$  (a measure of catalytic activity by normalizing current to the geometric surface area of the electrode) in acidic solution (left) and alkaline solution (right), respectively. The results show that the catalytic activity trends in both acidic and alkaline media are broadly in line with the trends predicted by the theoretical results. In order to better reflect the catalytic activities, we normalize the current densities by the BET surface areas of MB<sub>2</sub>, and then try to correlate the required overpotentials at a normalized current density of  $0.1 \text{ mA cm}^{-2}$  with the calculated  $d$ -band center values. As shown in **Figure 4b,c**, the trends in catalytic activity are almost linearly described by the  $d$ -band centers of MB<sub>2</sub>, well in agreement with the predicted activity trends (**Figure 2a**). These results suggest that the calculated  $d$ -band center is a reliable descriptor for elucidating the catalytic activity of MB<sub>2</sub> for HER. Compared with the typical descriptor ( $\Delta G_{\text{H}^*}$ ),  $d$ -band center is more intrinsically relevant to material properties and can be more easily calculated. These features

render  $d$ -band center a predictive power to quickly evaluate catalytic activity and guide the rational design of new catalysts.

As revealed in **Figure 4a**, RuB<sub>2</sub> exhibits the highest HER catalytic activity among these MB<sub>2</sub> as predicted, in both acidic and alkaline solutions. Specifically, RuB<sub>2</sub> requires very small overpotentials of 18 and 28 mV to generate a current density of  $10 \text{ mA cm}^{-2}$  in acidic and alkaline solutions, respectively. To achieve  $10 \text{ mA cm}^{-2}$  current density, the overpotential required by RuB<sub>2</sub> in acidic solution is quite close to that (17 mV) needed by the commercially available 20 wt% Pt/C (**Figure 5a**), while its overpotential in alkaline solution even lower than that required by the Pt/C catalyst (37 mV) (**Figure 5b**). The Pt-like activity of RuB<sub>2</sub> is further supported by comparing the Tafel slopes of RuB<sub>2</sub> and Pt/C, which are 38.9 and 31.6 mV per decade in acidic solution, respectively (**Figure S7a**, Supporting Information), and 28.7 and 29.5 mV per decade in alkaline solution, respectively (**Figure S7b**, Supporting Information). These comparisons demonstrate the outstanding activity of RuB<sub>2</sub>, suggesting that RuB<sub>2</sub> may be a potential replacement for the Pt-based catalysts. Besides good catalytic activity, RuB<sub>2</sub> also exhibits good catalytic stability for HER in both acidic and alkaline solution. After 50 h-long electrocatalysis at  $10 \text{ mA cm}^{-2}$  current density in either acidic solution or in alkaline solution, RuB<sub>2</sub> still remains catalytic activity and microstructures

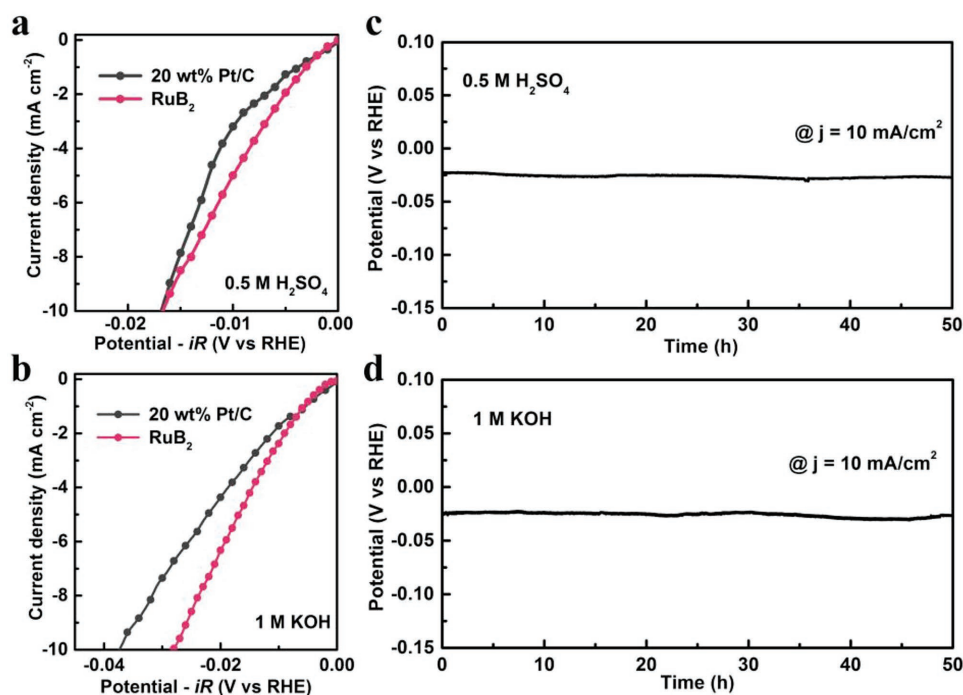


**Figure 5.** a,b) Polarization curves after *iR* compensation for the RuB<sub>2</sub> and 20 wt% Pt/C in 0.5 M H<sub>2</sub>SO<sub>4</sub> solution and 1.0 M KOH solution; c,d) Chronopotentiometric curves with RuB<sub>2</sub> for HER at a current density of 10 mA cm<sup>-2</sup> (without *iR*-correction) in 0.5 M H<sub>2</sub>SO<sub>4</sub> solution and 1.0 M KOH solution.

unchanged (Figure 5c,d and Figure S8, Supporting Information). The faradaic efficiency measurements in both acidic and alkaline solution (see Figure S9 in the Supporting Information) present that actual H<sub>2</sub> yield based on RuB<sub>2</sub> catalyst is nearly 100%, indicating a total electricity-to-hydrogen conversion during electrocatalysis.

In order to further understand the better catalytic activity of RuB<sub>2</sub> compared to Pt in alkaline solution, we investigate the reaction pathway for water dissociation on the RuB<sub>2</sub>(001) and Pt(111) surfaces by DFT calculation because water dissociation has been proven to be important for HER in alkaline medium.<sup>[2a,16]</sup> Typically, water dissociation involves three steps (Figure 6 and Figures S10, S11, Supporting Information): i) in initial state (IS), water molecule prefers to adsorbing on a Ru top site on the RuB<sub>2</sub>(001) surface and a Pt top site on the Pt(111) surface, respectively; ii) in transition state (TS), the water molecule breaks up into OH\* and H\* species by an O–H bond breaking process; iii) in final state (FS), H atom moves to a B–B bridge site on the RuB<sub>2</sub>(001) surface and a Pt top site on the Pt(111) surface, respectively. The calculation results (Figure 5) show that the activation energy of O–H bond breaking on RuB<sub>2</sub>(001) surface (0.64 eV) is smaller than that on Pt(111) surface (0.85 eV), indicating that water dissociation is kinetically more favorable for RuB<sub>2</sub>

relative to Pt. In addition, the FS of water dissociation for the RuB<sub>2</sub>(001) surface is obviously thermodynamically more stable than that for the Pt(111) surface, as revealed by the adsorption energy of the former (−0.96 eV) significantly lower than that of the later (0.05 eV). These findings overall demonstrate that

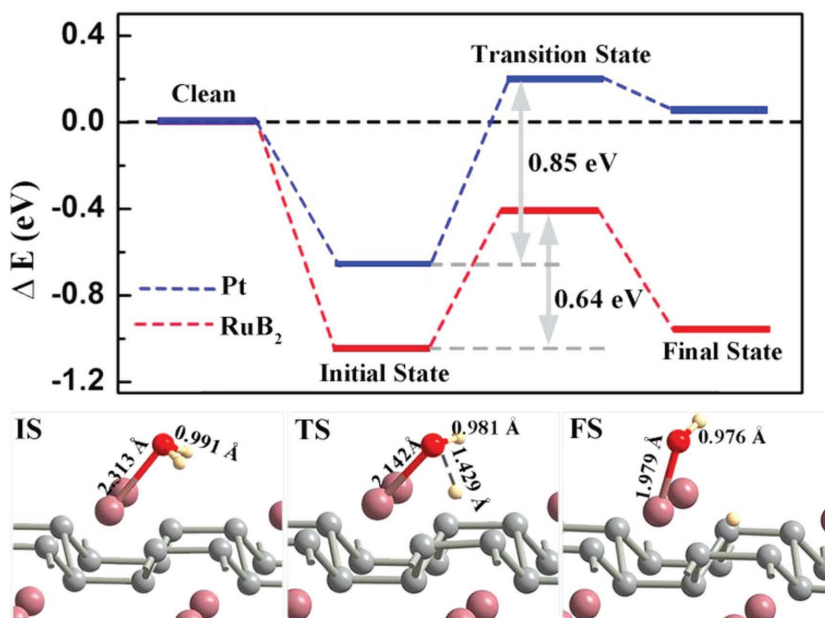


**Figure 6.** Reaction pathways for water molecule dissociation on the RuB<sub>2</sub>(001) and Pt(111) surfaces. Optimized structures for water molecule dissociation on the RuB<sub>2</sub>(001) surface in the IS, TS, and FS are shown in the side views.

RuB<sub>2</sub> possesses more favorable surfaces for water dissociation in comparison with Pt, thereby facilitating the alkaline HER electrocatalysis.

### 3. Conclusion

In summary, we have demonstrated that *d*-band center can be used as a reliable descriptor to reflect catalytic activity for HER of metal diboride. This descriptor helps us to establish the clear activity trends for a family of transition metal diboride in catalyzing HER. We have identified theoretically and experimentally, based on the activity trends, that RuB<sub>2</sub> with optimized *d*-band center and high density of efficient active sites is the most competitive, nonplatinum candidate among metal diborides for HER. Our findings advance the fundamental understanding of electronic structure effects on catalytic process of metal borides, and provide a promising descriptor-based design principle for better screening of advanced materials with improved HER activity.

### 4. Theoretical Section

**Computation Details:** The generalized gradient approximation (GGA) with the Perdew–Burke–Ernzerhof (PBE) exchange–correlation functional<sup>[17]</sup> and a 400 eV cutoff for the plane-wave basis set<sup>[18]</sup> were employed to perform all the DFT computations of the materials within the frame of Vienna ab initio simulation package (VASP).<sup>[19]</sup> The Brillouin zones were sampled by Monkhorst–Pack 9 × 9 × 9 and 5 × 5 × 1 k-point grid for all geometric optimization of bulk and slab models, and 7 × 7 × 1 k-point grid was used to calculate the DOS of slab models.<sup>[20]</sup> For all theoretical models, the convergence threshold was set as 10<sup>−4</sup> eV in energy and 0.02 eV Å<sup>−1</sup> in force. The correction of van der Waals interaction was included using the DFT-D2 method.<sup>[21]</sup> The symmetrization was switched off and the dipolar correction was included.

For the slab models of MB<sub>2</sub>, we chose (001) surface with metal-termination and 2 × 2 repeated unit cell and eight atom layers. The models of Pt(111) and Ru(0001) contain four atom layers. The 15 Å vacuum layer was selected to avoid interlayer interactions. All the upper half of atom layers were fully relaxed and the remaining were kept frozen during computational process.

**Computations of Free-Energy for the Hydrogen Evolution Reaction:** The Gibbs free-energy of H\* (ΔG<sub>H\*</sub>) was calculated by the equation ΔG<sub>H\*</sub> = ΔE<sub>H\*</sub> + ΔZPE − TΔS, where ΔE<sub>H\*</sub>, ΔZPE, and ΔS are the adsorption energy, zero point energy, and entropy change.<sup>[12e]</sup> ΔZPE was obtained by ΔZPE = ZPE (H\*) − 1/2 ZPE (H<sub>2</sub>), and in special, ΔS was obtained by ΔS = S(H\*) − 1/2 S(H<sub>2</sub>) ≈ −1/2 S(H<sub>2</sub>) because of negligible vibrational entropy of H\*. At 300 K and 1 atm, TS(H<sub>2</sub>) = 0.41 eV, thus TΔS = −0.205 eV. Tables S1–S4 in the Supporting Information show the ΔE<sub>H\*</sub> of different materials at different sites.

We chose the most stable adsorption sites to investigate the hydrogen coverage θ<sub>H\*</sub> how to influence the ΔG<sub>H\*</sub>. θ<sub>H\*</sub> is defined as *n*/*N*, where *n* is number of H\* on the surface and *N* is the number of surface metal atom in the slab models. At different θ<sub>H\*</sub>, ΔE<sub>H\*</sub> can be calculated by Equation (1):

$$\Delta E_{H^*} = E(\text{surface} + nH) - E[\text{surface} + (n-1)H] - 1/2 E(H_2) \quad (1)$$

where *E* (surface + *n*H) and *E* [surface + (*n*−1) H] are the energy of *n* and *n*−1 H atom adsorbing on the surface. *E* (H<sub>2</sub>) is the energy of hydrogen molecule in the gas phase. Table S5 in the Supporting Information shows the ΔG<sub>H\*</sub> at different hydrogen coverages for different materials.

**Density of States and *d*-Band Center Computation:** In the *d*-band model of adsorption,<sup>[22]</sup> the adsorption energy can be described as Equation (2):

$$\Delta E = \Delta E_{sp} + \Delta E_d \quad (2)$$

where ΔE<sub>sp</sub> is adsorption energy contribution from *sp* electrons and ΔE<sub>d</sub> is energy contribution from *d* electrons. In the simplest form, ΔE<sub>sp</sub> was assumed as constant for all transition metals. Thus, the *d*-band electronic structure of transition metal is crucial for adsorption energy of adsorbate. The simplest model to describe the *d* band is *d*-band center. It can be obtained by<sup>[23]</sup>:

$$\epsilon_d = \frac{\int_{-\infty}^{\infty} n_d(\epsilon) \epsilon d\epsilon}{\int_{-\infty}^{\infty} n_d(\epsilon) d\epsilon} \quad (3)$$

where ε is energy referring to E-Fermi and *n<sub>d</sub>* (ε) is DOS projected onto *d*-states. Moreover, the width and shape of *d*-band also influence the adsorbate. The second moment of ε<sub>d</sub>, the width of the *d*-band, can be obtained by<sup>[23]</sup>:

$$\epsilon_d^2 = \frac{\int_{-\infty}^{\infty} n_d(\epsilon) (\epsilon - \epsilon_d)^2 d\epsilon}{\int_{-\infty}^{\infty} n_d(\epsilon) d\epsilon} \quad (4)$$

The *d*-band filling can be calculated by integrating the *n<sub>d</sub>* (ε) up to Fermi level<sup>[24]</sup>:

$$N_d = \int_{-\infty}^0 n_d(\epsilon) d\epsilon \quad (5)$$

**Water Dissociation Reaction on the Pt(111) and RuB<sub>2</sub>(001) Surfaces:** We studied the favorable configurations and energetics of adsorption of molecular H<sub>2</sub>O and OH + H pairs on Pt (111) and RuB<sub>2</sub> (001) at different sites. The adsorptions of molecular H<sub>2</sub>O and OH + H pairs were taken as IS and FS of the water dissociation reaction (H<sub>2</sub>O\* → OH\* + H\*). The TS of reaction was obtained by the nudged-elastic band (NEB) and climbing image NEB (CI-NEB) method,<sup>[25]</sup> then confirmed by following vibrational frequency analysis. Figures S10 and S11 in the Supporting Information show the optimized adsorption structures for the IS, TS, and FS of the most favorable path on the Pt(111) and RuB<sub>2</sub>(001) surfaces. The adsorption energy (*E<sub>ads</sub>*) of all states and activation energies (*E<sub>a</sub>*) were calculated by Equations (6) and (7):

$$E_{ads} = E_{sur+ads} - E_{sur} - E_{water} \quad (6)$$

$$E_a = E_{TS} - E_{ini} \quad (7)$$

*E<sub>water</sub>* is isolated water molecule energy and *E<sub>sur</sub>* is energy of the substrate without any adsorbate. *E<sub>sur+ads</sub>* is the energy of the

substrate with adsorbate.  $E_{\text{ini}}$  and  $E_{\text{fin}}$  is the energy of molecular and dissociative adsorption of water on the substrate.

## 5. Experimental Section

**Chemicals and Reagents:** Titanium(IV) chloride ( $\text{TiCl}_4$ , 99.0%, AR), Zirconium(IV) chloride ( $\text{ZrCl}_4$ , 98%), Niobium(V) chloride ( $\text{NbCl}_5$ , 99%), Tungsten(VI) hexachloride ( $\text{WCl}_6$ , 99.9%), Molybdenum(V) chloride ( $\text{MoCl}_5$ , 99.6%), Cobalt(II) chloride ( $\text{CoCl}_2$ , 99.7%), Potassium hexachloroosmate(IV) ( $\text{K}_2\text{OsCl}_6$ , Os 38.7%), Manganese(II) chloride ( $\text{MnCl}_2$ , 99%), and Potassium aquapentachlororuthenate(III) ( $\text{K}_2\text{RuCl}_5$ ) were purchased from Aladdin Chemistry Co., Ltd. Hafnium(IV) chloride ( $\text{HfCl}_4$ , 99.5%), Chromium(II) chloride ( $\text{CrCl}_2$ , 97%), and Tantalum(V) chloride ( $\text{TaCl}_5$ , 98%) were purchased from Shanghai Macklin Biochemical Co., Ltd. Vanadium(III) chloride ( $\text{VCl}_3$ , 99%) was purchased from Sinopharm Chemical Reagent Co., Ltd. Potassium hexachlororhenate(IV) ( $\text{K}_2\text{ReCl}_6$ , 99.9%), Iron(II) chloride ( $\text{FeCl}_2$ , 99.5%), and Magnesium diborides ( $\text{MgB}_2$ ) were purchased from Alfa Aesar Chemicals Co., Ltd. Isopropanol, sulfuric acid ( $\text{H}_2\text{SO}_4$ ), and potassium hydroxide (KOH) were purchased from Beijing Chemical Factory. Platinum on graphitized carbon (20 wt% Pt/C) and Nafion perfluorinated resin solution were purchased from Sigma-Aldrich. Highly purified water (>18 M $\Omega$  cm resistivity) was obtained from a PALL PURELAB Plus system.

**Synthesis of Transition Metal Borides:** All transition metal diborides were synthesized by quasi SSM reaction.<sup>[14]</sup> To avoid moisture influence, all the chemicals were weighed under infrared light. First, a certain amount of anhydrous metal source and magnesium diboride ( $\text{MgB}_2$ ) were placed into a quartz tube, which was then sealed in a vacuum atmosphere (0.9 Pa). Note that  $\text{TiCl}_4$  is liquid, so freezing is required during vacuum operation. Next, the sealed quartz tube was transformed into a tube furnace to heat at a certain temperature with a heating rate of 2 °C min<sup>-1</sup>, and maintaining enough time (the detailed synthesis parameters are shown in Table S6 in the Supporting Information). After cooling to room temperature, the obtained black product was ground into powder and dispersed in a cleaning solution for 3 h post-treatment to remove by-product. Note that the majority of  $\text{MB}_2$  products were dispersed in 0.5 M  $\text{H}_2\text{SO}_4$  solution for the post-treatment, with the exception of  $\text{CrB}_2$  product dispersed in water for the post-treatment because  $\text{CrB}_2$  is soluble in acidic solution. Finally, the resulting sample was washed, and then oven-dried at 80 °C.

**Characterizations:** Powder X-ray diffraction (XRD) of the samples were recorded on a Rigaku D/Max 2550 X-ray diffractometer with a scan speed of 8° min<sup>-1</sup> within the diffraction angle range from 10°–80°. The specific surface area was obtained using the BET method on a Micromeritics ASAP 2020 M system. The TEM images were performed with a Philips-FEI Tecnai G2STwin microscope equipped with a field emission gun operating at 200 kV.

**Electrochemical Measurements:** A CH Instrument (Model 660E) was used with standard three-electrode system to perform electrochemical measurements. Carbon rod was used as the counter electrode. Saturated calomel electrodes (SCE) and Hg/HgO electrode were used as the reference electrode in acid condition (0.5 M  $\text{H}_2\text{SO}_4$  solution) and alkaline condition (1.0 M KOH solution), respectively. Glassy carbon electrode (GCE) prepared with obtained materials (i.e.,  $\text{MB}_2$ ) was used as the working electrodes. To prepare the working electrode: 1) 8 mg of catalyst was uniformly dispersed in 400  $\mu\text{L}$  of isopropanol and 400  $\mu\text{L}$  of conductive polymer binder (0.3% Nafion solution); 2) 2  $\mu\text{L}$  of this solution was dropped onto a GCE with a diameter of 3 mm, and then dried in the air. The loading mass was 0.281 mg cm<sup>-2</sup> on the GCE; and 3) 2  $\mu\text{L}$  of 0.3% Nafion solution was dropped on top and dried. The working electrodes were tested in 0.5 M  $\text{H}_2\text{SO}_4$  and 1.0 M KOH solutions. During the measurements,  $\text{N}_2$  was continuously passed into the electrochemical cell. Linear sweep voltammetry (LSV) measurements were performed with the scan rate of 0.5 mV s<sup>-1</sup> and 85% *iR*-correction. In order to determine the stability of the catalyst,

chronopotentiometric measurements were performed at a current density of 10 mA cm<sup>-2</sup> without *iR*-correction. The potential was converted to the potential versus the reversible hydrogen electrode (RHE) in acidic condition according to Equation (8), in alkaline condition according to Equation (9):

$$E_{\text{vs RHE}} = E_{\text{vs SCE}} + E_{\text{SCE}}^0 + 0.059\text{pH} \quad (8)$$

$$E_{\text{vs RHE}} = E_{\text{vs Hg/HgO}} + E_{\text{Hg/HgO}}^0 + 0.059\text{pH} \quad (9)$$

In order to confirm the Faradic efficiency during HER catalysis, the  $\text{H}_2$  gas generated was collected by a water drainage method and its amount (in mol) was calculated using the ideal gas law. The theoretical value was calculated by assuming that 100% of the current output during the HER reaction. Faradic efficiency was then obtained by calculating the ratio of the amount of  $\text{H}_2$  evolved during the HER to the amount of  $\text{H}_2$  expected to generate based on theoretical considerations.

All reference electrodes were calibrated according to the method reported by Boettcher and co-workers.<sup>[26]</sup> First, two Pt electrodes were cleaned and cycled in 0.5 M  $\text{H}_2\text{SO}_4$  solution (about  $\pm 2$  V), and then as working electrode and counter electrode. The electrolyte was saturated with hydrogen before use and hydrogen was bubbled over the working electrode during the test. The wide-ranged LSV was measured in a cathode to determine possible zero current potential. Then controlled-potential chronoamperometric tests were performed to further determine the zero current potential. It was necessary to stabilize for 300 s to reach the steady state value under each potential.

The  $j_{\text{BET}}$  value was normalized with the BET surface area from Equation (10):

$$j_{\text{BET}} = \frac{i \times 100}{S \times m_{\text{loading}} \times A_{(\text{BET})}} \quad (10)$$

where  $i$  is the current obtained with 85% *iR*-correction;  $S$  is the geometric area of GCE (0.071 cm<sup>2</sup>);  $m_{\text{loading}}$  is the loading mass of metal borides (0.281 mg cm<sup>-2</sup>);  $A_{(\text{BET})}$  is the BET surface area of metal borides (m<sup>2</sup> g<sup>-1</sup>).

## Supporting Information

Supporting Information is available from the Wiley Online Library or from the author.

## Acknowledgements

Q.L., X.Z., and X.A. contributed equally to this work. X.Z. acknowledges the financial support from National Key R&D Program of China, Grant No. 2017YFA0207800, National Natural Science Foundation of China (NSFC) Grant No. 21771079, Jilin Province Science and Technology Development Plan 20170101141JC, Young Elite Scientist Sponsorship Program by CAST, Program for JLU Science and Technology Innovative Research Team (JLUSTIRT) and Fok Ying Tung Education Foundation, Grant No.161011. H.C. acknowledges the financial support from Postdoctoral Innovative Talent Support Program (Grant No. BX20180120) and China Postdoctoral Science Foundation (Grant No. 2018M641771). This work is also supported by the National Natural Science Foundation of China (Grant No. 21621001) and the 111 Project (No. B17020).

## Conflict of Interest

The authors declare no conflict of interest.



## Keywords

*d*-band center, electrocatalysis, hydrogen evolution reaction, metal diboride, non-Pt catalysts

Received: October 31, 2018

Revised: November 18, 2018

Published online: December 10, 2018

- [1] a) X. Zou, Y. Zhang, *Chem. Soc. Rev.* **2015**, 44, 5148; b) Z. W. Seh, J. Kibsgaard, C. F. Dickens, I. Chorkendorff, J. K. Nørskov, T. F. Jaramillo, *Science* **2017**, 355, eaad4998; c) Y. Zheng, Y. Jiao, M. Jaroniec, S. Z. Qiao, *Angew. Chem., Int. Ed.* **2015**, 54, 52.
- [2] a) R. Subbaraman, D. Tripkovic, D. Strmcnik, K. C. Chang, M. Uchimura, A. P. Paulikas, V. Stamenkovic, N. M. Markovic, *Science* **2011**, 334, 1256; b) P. T. Wang, X. Zhang, J. Zhang, S. Wan, S. J. Guo, G. Lu, J. L. Yao, X. Q. Huang, *Nat. Commun.* **2017**, 8, 14580; c) P. T. Wang, K. Z. Jiang, G. M. Wang, J. L. Yao, X. Q. Huang, *Angew. Chem., Int. Ed.* **2016**, 55, 12859; d) T. T. Chao, X. Luo, W. X. Chen, B. Jiang, J. J. Ge, Y. Lin, G. Wu, X. Q. Wang, Y. M. Hu, Z. B. Zhuang, Y. Wu, X. Hong, Y. D. Li, *Angew. Chem., Int. Ed.* **2017**, 56, 16047.
- [3] a) M. A. Lukowski, A. S. Daniel, F. Meng, A. Forticaux, L. S. Li, S. Jin, *J. Am. Chem. Soc.* **2013**, 135, 10274; b) D. Voiry, H. Yamaguchi, J. W. Li, R. Silva, D. C. B. Alves, T. Fujita, M. W. Chen, T. Asefa, V. B. Shenoy, G. Eda, M. Chhowalla, *Nat. Mater.* **2013**, 12, 850; c) J. X. Feng, J. Q. Wu, Y. X. Tong, G. R. Li, *J. Am. Chem. Soc.* **2018**, 140, 610.
- [4] a) H. Vrubel, X. L. Hu, *Angew. Chem.* **2012**, 124, 12875; b) Z. C. Zhuang, Y. Li, Z. L. Li, F. Lv, Z. Q. Lang, K. N. Zhao, L. Zhou, L. Moskalova, S. J. Guo, L. Q. Mai, *Angew. Chem.* **2018**, 130, 505; c) H. B. Wu, B. Y. Xia, L. Yu, X. Y. Yu, X. W. Lou, *Nat. Commun.* **2015**, 6, 6512.
- [5] a) E. J. Popczun, J. R. McKone, C. G. Read, A. J. Biacchi, A. M. Wiltrout, N. S. Lewis, R. E. Schaak, *J. Am. Chem. Soc.* **2013**, 135, 9267; b) Q. Liu, J. Q. Tian, W. Cui, P. Jiang, N. Y. Cheng, A. M. Asiri, X. P. Sun, *Angew. Chem., Int. Ed.* **2014**, 53, 6710; c) J. X. Feng, S. Y. Tong, Y. X. Tong, G. R. Li, *J. Am. Chem. Soc.* **2018**, 140, 5118.
- [6] a) Z. Y. Chen, Y. Song, J. Y. Cai, X. S. Zheng, D. D. Han, Y. S. Wu, Y. P. Zang, S. W. Niu, Y. Liu, J. F. Zhu, X. J. Liu, G. M. Wang, *Angew. Chem., Int. Ed.* **2018**, 57, 5076; b) R. Wu, J. F. Zhang, Y. M. Shi, D. L. Liu, B. Zhang, *J. Am. Chem. Soc.* **2015**, 137, 6983; c) Y. W. Liu, X. M. Hua, C. Xiao, T. F. Zhou, P. C. Huang, Z. P. Guo, B. C. Pan, Y. Xie, *J. Am. Chem. Soc.* **2016**, 138, 5087; d) X. Zhang, Z. M. Luo, P. Yu, Y. Q. Cai, Y. H. Du, D. X. Wu, S. Gao, C. L. Tan, Z. Li, M. Q. Ren, T. Osipowicz, S. M. Chen, Z. Jiang, J. Li, Y. Huang, J. Yang, Y. Chen, C. Y. Ang, Y. L. Zhao, P. Wang, L. Song, X. J. Wu, Z. Liu, A. Borgna, H. Zhang, *Nat. Catal.* **2018**, 1, 460.
- [7] a) S. Y. Nong, W. J. Dong, J. W. Yin, B. W. Dong, Y. Lu, X. T. Yuan, X. Wang, K. J. Bu, M. Y. Chen, S. D. Jiang, L. M. Liu, M. L. Sui, F. Q. Huang, *J. Am. Chem. Soc.* **2018**, 140, 5719; b) J. X. Feng, H. Xu, Y. T. Dong, X. F. Lu, Y. X. Tong, G. R. Li, *Angew. Chem., Int. Ed.* **2017**, 56, 2960; c) Z. H. Pu, I. S. Amiin, Z. K. Kou, W. Q. Li, S. C. Mu, *Angew. Chem., Int. Ed.* **2017**, 56, 11559; d) H. H. Duan, D. G. Li, Y. Tang, Y. He, S. F. Ji, R. Y. Wang, H. F. Lv, P. P. Lopes, A. P. Paulikas, H. Y. Li, S. X. Mao, C. M. Wang, N. M. Markovic, J. Li, V. R. Stamenkovic, Y. D. Li, *J. Am. Chem. Soc.* **2017**, 139, 5494.
- [8] B. Hinnemann, P. G. Moses, J. Bonde, K. P. Jørgensen, J. H. Nielsen, S. Hørch, I. Chorkendorff, J. K. Nørskov, *J. Am. Chem. Soc.* **2005**, 127, 5308.
- [9] a) Y. L. Chen, G. T. Yu, W. Chen, Y. P. Liu, G. D. Li, P. W. Zhu, Q. Tao, Q. J. Li, J. W. Liu, X. P. Shen, H. Li, X. R. Huang, D. J. Wang, T. Asefa, X. Zou, *J. Am. Chem. Soc.* **2017**, 139, 12370; b) H. Park, A. Encinas, J. P. Scheifers, Y. M. Zhang, B. P. T. Fokwa, *Angew. Chem., Int. Ed.* **2017**, 56, 5575.
- [10] G. Akopov, M. T. Yeung, R. B. Kaner, *Adv. Mater.* **2017**, 29, 1604506.
- [11] a) J. K. Nørskov, F. Studt, F. Abild-Pedersen, T. Bligaard, in *Fundamental Concepts in Heterogeneous Catalysis* (Eds: J. K. Nørskov, F. Studt, F. Abild-Pedersen, T. Bligaard), John Wiley & Sons, Inc., Hoboken, NJ, USA **2014**, pp. 114–137; b) B. Hammer, J. K. Nørskov, in *Advances in Catalysis*, Vol. 45 (Eds: B. C. Gates, H. Knozinger), Elsevier Inc., Aalborg, Denmark **2000**, pp. 71–129.
- [12] a) E. Skúlason, V. Tripkovic, M. E. Björketun, S. Gudmundsdóttir, G. Karlberg, J. Rossmeisl, T. Bligaard, H. Jónsson, J. K. Nørskov, *J. Phys. Chem. C* **2010**, 114, 18182; b) P. J. Feibelman, *Science* **2002**, 295, 99; c) M. Pachecka, J. M. Sturm, C. J. Lee, F. Bijkerk, *J. Phys. Chem. C* **2017**, 121, 6729; d) Á. Logadóttir, J. K. Nørskov, *J. Catal.* **2003**, 220, 273; e) J. K. Nørskov, T. Bligaard, A. Logadóttir, J. R. Kitchin, J. G. Chen, S. Pandalov, U. Stimming, *J. Electrochem. Soc.* **2005**, 152, J23.
- [13] a) P. R. Jothi, K. Yubuta, B. P. T. Fokwa, *Adv. Mater.* **2018**, 30, 1704181; b) S. Carenco, D. Portehault, C. Boissière, N. Mézailles, C. Sanchez, *Chem. Rev.* **2013**, 113, 7981.
- [14] a) L. P. Parkin, *Chem. Soc. Rev.* **1996**, 25, 199; b) E. G. Gillan, R. B. Kaner, *Chem. Mater.* **1996**, 8, 333.
- [15] a) Y. C. Liang, Z. B. Wu, X. Yuan, W. Q. Zhang, P. H. Zhang, *Nanoscale* **2016**, 8, 1055; b) H. P. Woods, F. E. Wawner, B. G. Fox, *Science* **1966**, 151, 75.
- [16] a) N. Danilovic, R. Subbaraman, D. Strmcnik, K. C. Chang, A. P. Paulikas, V. R. Stamenkovic, N. M. Markovic, *Angew. Chem., Int. Ed.* **2012**, 51, 12495; b) Y. Zheng, Y. Jiao, A. Vasileff, S. Z. Qiao, *Angew. Chem., Int. Ed.* **2018**, 57, 7568.
- [17] J. P. Perdew, K. Burke, M. Ernzerhof, *Phys. Rev. Lett.* **1996**, 77, 3865.
- [18] P. E. Blöchl, *Phys. Rev. B* **1994**, 50, 17953.
- [19] a) G. Kresse, J. Furthmüller, *Comput. Mater. Sci.* **1996**, 6, 15; b) G. Kresse, J. Furthmüller, *Phys. Rev. B* **1996**, 54, 11169.
- [20] H. J. Monkhorst, J. D. Pack, *Phys. Rev. B* **1976**, 13, 5188.
- [21] S. Grimme, *J. Comput. Chem.* **2006**, 27, 1787.
- [22] T. Bligaard, J. K. Nørskov, *Electrochim. Acta* **2007**, 52, 5512.
- [23] A. Vojvodic, J. K. Nørskov, F. Abild-Pedersen, *Top. Catal.* **2014**, 57, 25.
- [24] J. R. Kitchin, J. K. Nørskov, M. A. Barteau, J. G. Chen, *J. Chem. Phys.* **2004**, 120, 10240.
- [25] G. Henkelman, P. Uberuaga, H. Jónsson, *J. Chem. Phys.* **2000**, 113, 9901.
- [26] M. B. Stevens, L. J. Enman, A. S. Batchellor, M. R. Vise, A. E. Cosby, C. D. M. Trang, S. W. Boettcher, *Chem. Mater.* **2017**, 29, 120.